Int J Appl Earth Obs Geoinformation 85 (2020) 101991

Contents lists available at ScienceDirect

Int J Appl Earth Obs Geoinformation

journal homepage: www.elsevier.com/locate/jag

The application of day and night time ASTER satellite imagery for geothermal and mineral mapping in East Africa

Rob Hewson[a,*], Elisante Mshiu[b], Chris Hecker[a], Harald van der Werff[a], Frank van Ruitenbeek[a], Dinand Alkema[a], Freek van der Meer[a]

[a] ITC, University of Twente, Enschede, the Netherlands
[b] Dept of Geology, University of Dar Es Salaam, Dar Es Salaam, Tanzania

ARTICLE INFO

Keywords:
Geothermal
ASTER
Mineral mapping
East Africa
Land surface temperature

ABSTRACT

There is considerable interest in optimizing geothermal exploration techniques via the mapping of alteration and evaporate mineralisation, as well as of thermal emissions associated with geothermally active areas on the Earth's surface. Optical and thermal satellite sensor technologies, improvements in processing algorithms and the means for large scale (e.g. 1:250,000) spatial data distribution are required for detecting both these attributes. The extensive visible, -near, -shortwave and thermal infrared (VNIR-SWIR-TIR) data archive acquired by the multi-spectral Advanced Spaceborne Thermal Emission Reflectance Radiometer (ASTER) provides a rich source of geoscience related imagery for geothermal exploration. Examples of generating large scale mosaicked ASTER imagery to provide province to continental mineral mapping have been undertaken in areas including such as Australia, western USA, Namibia and Zagros Mountains Iran. In addition, ASTER's thermal infrared imagery also provides night time land surface temperature (LST) estimates relevant for detecting possible geothermal related anomalies.

This study outlines existing methods for the application of ASTER data for geothermal exploration in East Africa. The study area encompasses a section of the East African Rift System across the Tanzanian and Kenyan border. The area includes rugged volcanic terrain which has had geological mapping of limited coverage at detailed scales, from various heritages and mapping agencies. This study summarizes the technology, the processing methodology and initial results in applying ASTER imagery for such compositional and thermal anomaly mapping related to geothermal activity. Fields observations have been used from the geothermal springs of Lake Natron, Tanzania, and compared with ASTER derived spectral composition and land surface temperature results. Published geothermal fields within the Kenyan portion of the study area have also been incorporated into this study.

1. Introduction

Spectroscopy Background and geothermal indicator mineral detection with ASTER

The results of fundamental research into mineral spectroscopy (Lyon and Burns, 1963; Adams and Filice, 1967; Hunt and Ashley, 1979; Vincent and Thomson, 1972; Vincent et al., 1975) laid the basis for later geological remote sensing and prompted the launch of such multi-spectral satellite sensors as NASA's Landsat TM (Thermatic Mapper) in the late 1980s' and ASTER in 1999 by Japan's METI (Ministry of Economy, Trade & Industry) and NASA (National Aeronautics & Space Administration). The relationship of the spectral bands of ASTER with common material spectral reflectance signatures are shown in Fig. 1. The freely available ASTER imagery has the advantage of additional thermal infrared bands. ASTER measures three bands within the VNIR (B1-B3) useful for detecting iron oxides and vegetation cover. In addition, six ASTER bands (B4-B9) observe within the SWIR wavelength region that includes the diagnostic clay / AlOH absorption feature centered at 2.2 um (e.g. kaolinite absorption within sandstone spectra, Fig. 1). ASTER SWIR bands 5, 6 and 7 have the potential to qualitatively detect changes in the AlOH/clay composition (e.g. Al content, or kaolinite/alunite versus muscovite or montmorillonite) from changes in the absorption feature wavelength shift. Abundance and compositional indices for minerals and/or mineral groups with absorption features such as AlOH, can be devised using such band ratios and relative band depth (RBD) arithmetic (Crowley et al., 1989).

* Corresponding author.
E-mail address: hewson001@gmail.com (R. Hewson).

https://doi.org/10.1016/j.jag.2019.101991
Received 28 June 2019; Received in revised form 6 October 2019; Accepted 17 October 2019
Available online 15 November 2019

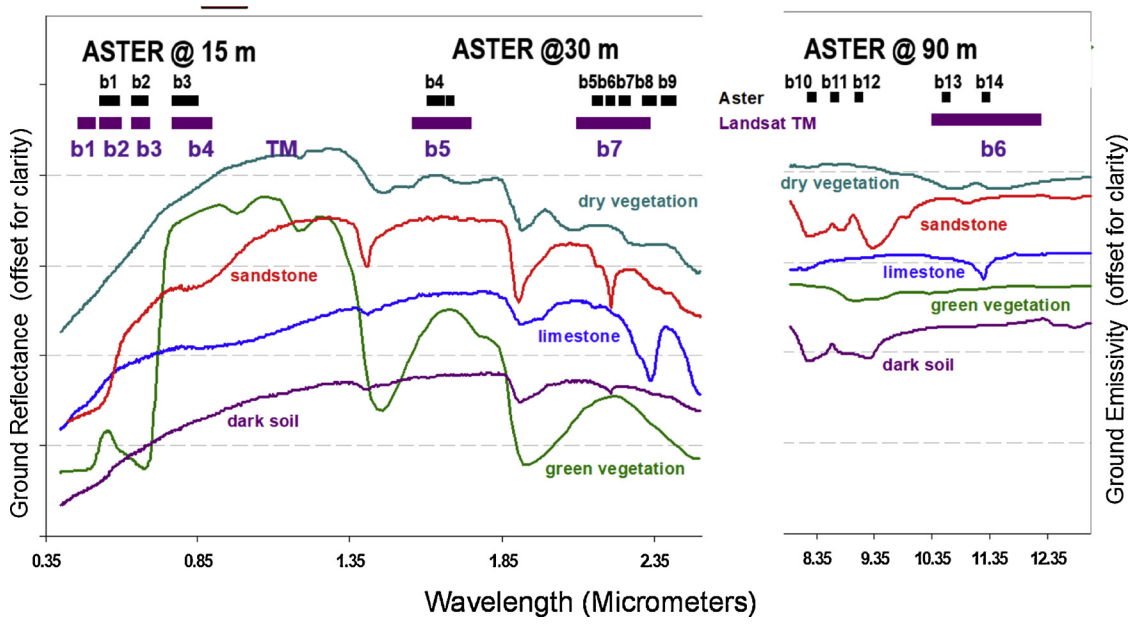

Fig. 1. Reflectance spectrum of common surface materials and ASTER's bands at these wavelengths.

Table 1
Key geothermal minerals and their representation with ASTER band parameters derived from the listed wavelength regions (Hecker et al., 2017).

Indicator Geothermal minerals	ASTER band parameter
Opaline silica	(B5 + B8) / (B6 + B7)
Alunite (Argillic)	B7 / B5 {Masked by higher values of AlOH/mica (B5 + B7) / B6}
Kaolinite (Argillic)	B7 / B5 {Masked by higher values of AlOH/mica (B5 + B7) / B6}
Chlorite / MgOH phyllosilicates	(B6 + B9) / (B7 + B8) {or (B6 + B9) / B8} ; {Masked by higher values B5 / B4 Ferrous}
Calcite	(B6 + B9) / (B7 + B8) {or (B6 + B9) / B8} {Masked by lower values of B5 / B4 Ferrous}

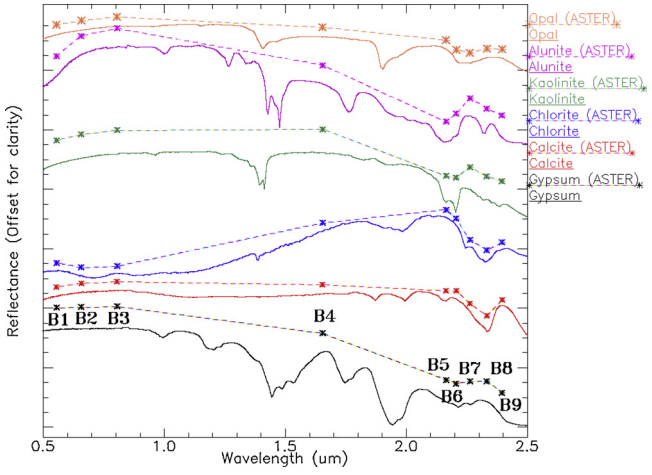

Fig. 2. USGS spectra of gypsum, calcite, chlorite kaolinite, alunite and opaline silica (Baldridge et al., 2009) and their ASTER resampled equivalent 0.5–2.5 u m and bands 1–9 shown.

Examples of using such ratios and RBDs for geothermal mineralization are demonstrated by (Hecker et al., 2017; Kratt et al., 2006a). Van der Meer (van der Meer et al., 2014) describes other indicator minerals associated with geothermal activity at various temperatures of formation however several require either thermal sensors and/or a higher spectral resolution. Table 1 summarizes some of the key geothermal minerals (Kratt et al., 2006a; van der Meer et al., 2014) and their calculation using ASTER band ratios. Example spectral signatures of such indicator minerals from the USGS (United States Geological Survey) VNIR-SWIR spectral library (Baldridge et al., 2009) are shown in Fig. 2 at laboratory and at equivalent ASTER band resolutions.

Since the release of ASTER satellite imagery in 2000, considerable compositional surface mapping has been achieved in many parts of the world (Abrams, 2000; Abrams et al., 2015). In particular, processing of ASTER Level 1B (e.g. radiance at sensor) and Level 2 (e.g. surface reflectance, surface kinetic temperature) products has provided regional mineral compositional information and land surface temperature (LST) data. Also, ASTER imagery with a swath width of 60 km has been acquired at spatial resolutions of 15 m (VNIR), 30 m (SWIR) and 90 m (TIR) (Abrams, 2000). ASTER currently continues to acquire VNIR and TIR imagery, except for the SWIR bands which failed from April 2008 due to sensor overheating issues (Abrams et al., 2015). Initially, geological mapping was undertaken with individual 60 by 60 km ASTER scenes. However, larger regional products (e.g. multiple 1:250,000 map size) were later generated via ASTER image mosaics for regions/provinces (Hewson et al., 2005), and more recently on a continental scale (Cudahy et al., 2016). This has provided added geological information for both mineral exploration companies and government agencies.

1.1. Detection of geothermal activity with ASTER TIR

Successful detection of some geothermal activity has been demonstrated with Landsat 8 TIRS (Thermal Infrared Sensor) data although requiring significant user input for the correction of the radiance imagery for atmospheric effects and temperature - emissivity separation processing within Dandong, China (Wang et al., 2019) and the Tulu Moye area of the Ethiopian Rift Valley (Darge et al., 2019). No diurnal temperature correction were applied in Tulu Moye case (Darge et al., 2019) whilst significant statistical processing and assumptions were

required for the day-night temperature correction in the Dandong case study (Wang et al., 2019).

ASTER's five band thermal radiance sensor has the potential to map the presence of hot springs, fumaroles and heated ground surfaces of 50^0 + C temperature (van der Meer et al., 2014). Like Landsat 8 with a spatial resolution of 100 m, ASTER's 90 m limits the detectability of localized hot springs and fumaroles. However night time ASTER acquisition has demonstrated an ability to identify and map such geothermal surface features in Flores Island, Indonesia (Urai et al., 2002) and also in Nevada, USA (Coolbaugh et al., 2007). In this study, geothermal anomalies refer to isolated temperature values, of more than one pixel, spatially coherent but above the background land surface temperature recorded by ASTER imagery. Utilizing ASTER for this mapping study also had the benefits of choosing up to 8 years combined optical VNIR-SWIR and 18 years TIR emission archived imagery, available at no cost. ASTER's TIR Level 2 LST product is also easily accessible and well validated (Abrams, 2000; Abrams et al., 2015). In this study additional pre-processing of the ASTER LST for topographic temperature effects (e.g. elevation, aspect) was applied as in previous studies, to enhance geothermal thermal related anomalies (Coolbaugh et al., 2007; Eneva et al., 2006).

1.2. Study objectives

This study aimed to investigate the feasibility of mapping both mineral composition and thermal anomalies associated with geothermal activity within the East Africa Rift using day and night time ASTER imagery (blue dashed box, Fig. 3) (Simiyu and Keller, 2000). In particular, the focus was to investigate the ability of ASTERs' VNIR-SWIR imagery in East Africa to provide supplementary geological information, including the geothermal indicator minerals of argillic (alunite, kaolinite) clays, calcite (travertine) and silica (opaline) deposits. This study will also attempt to map night time LST anomalies possibly associated with geothermal activity with ASTER's TIR sensor. The area contained several currently exploited Kenyan geothermal fields, including the Olkaria Power Plant, examined for its possible alteration and thermal response (red box, Fig. 3). This study also follows previous research by the authors in the general area, but was only using limited day-time ASTER derived products and did not examine the Kenyan Olkaria geothermal fields or the Lake Natron area in detail (Hewson et al., 2018).

2. Study area

The study area straddles the Kenyan and Tanzanian border and includes the large topographic relief associated with the East African Rift's main North-South graben feature (Fig. 3). The area included some of the established geothermal sites, including the major Olkaria geothermal field (red box, Fig. 3). Lake Natron within the East African Rift Valley of Tanzania was also examined (dashed green box, Fig. 3b).

This rift structure can be observed using the Shuttle Radar Topographic Mapper (SRTM) Digital Elevation Model (DEM) data, artificially shaded to enhance relief (Fig. 3b).

Interpreting areas for mineralogy formed from possible alteration is assisted by understanding the main host rock units present and their mineral composition. The overall study area straddles the Kenyan Tanzanian border area as shown (blue box, Figs. 3 and 4). The history and diversity of published geological mapping however is somewhat complicated by the areas' straddling of the border. Fig. 4 is designed to show cross border geological mapping issues, from a composite of the recent Minerogenic Map of Tanzania (Legler et al., 2015) and Kenyan geological mapping (ACP-INT: Secretariat of African, 2019). In

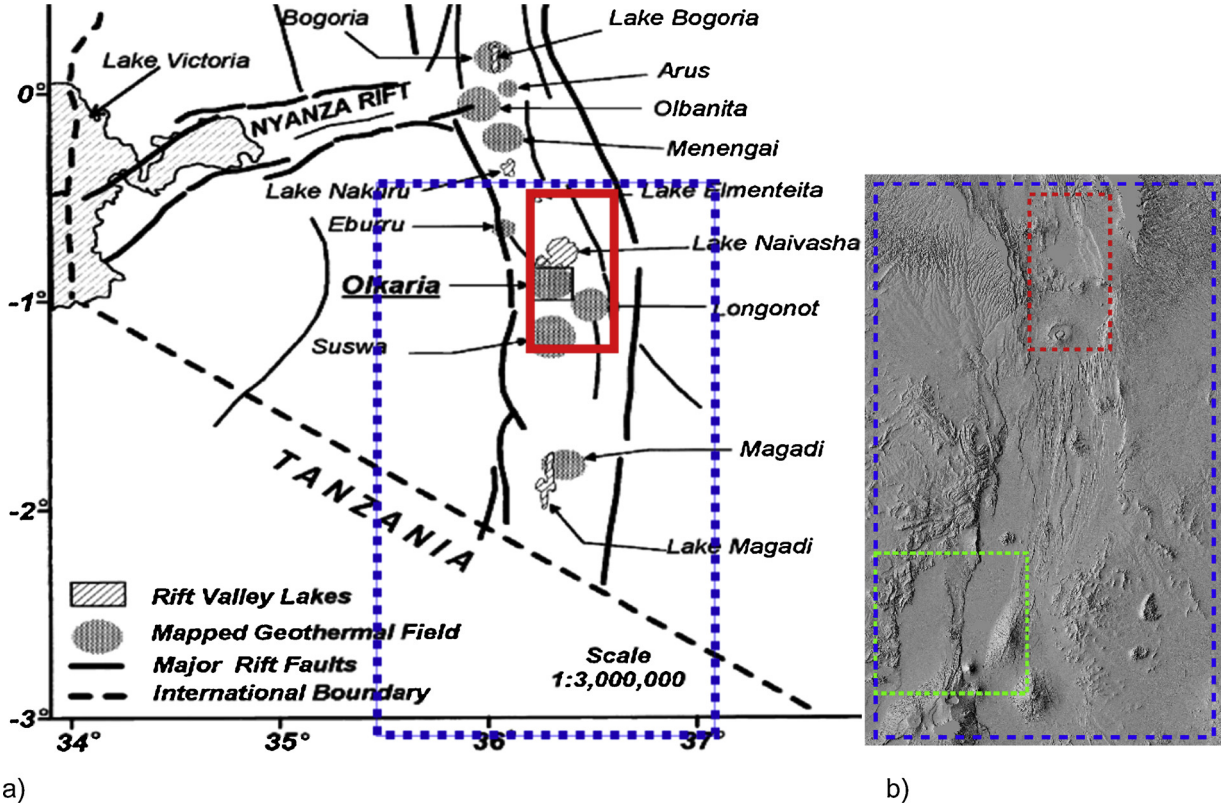

Fig. 3. a) Location of the overall study area (blue dashed box) and the Kenyan geothermal study area (red box) in relation to the Rift Valley and established geothermal fields, courtesy (Simiyu and Keller, 2000); b) Study areas shown in a) including the Lake Natron area (green dashed box) overlain over sun shaded SRTM DEM showing the north – north easterly trending Rift Valley with steep relief. (For interpretation of the references to colour in this figure legend, the reader is referred to the web version of this article).

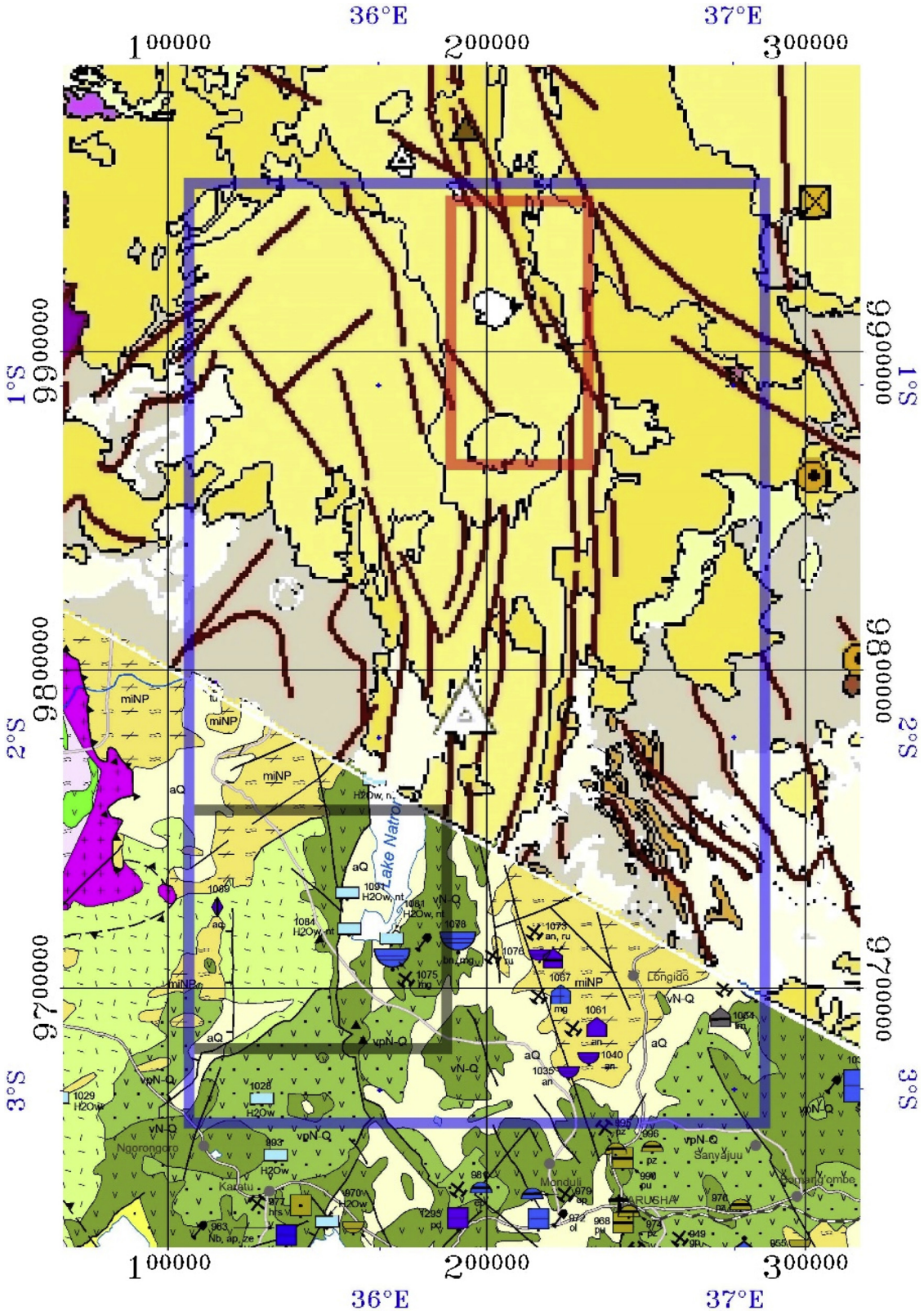

Fig. 4. Location of overall study area (blue box) in relation to examples of the geological mapping along the Rift Valley border region. Also highlights this investigations' Kenyan geothermal study area (red) and the Lake Natron geothermal spring area (black box). (For interpretation of the references to colour in this figure legend, the reader is referred to the web version of this article).

Note: the geological units shown are used simply to illustrate the variation of the published stratigraphic divisions across the study area. Tanzanian geology from (Legler et al., 2015) and the Kenyan geology composite (ACP-INT: Secretariat of African, 2019).

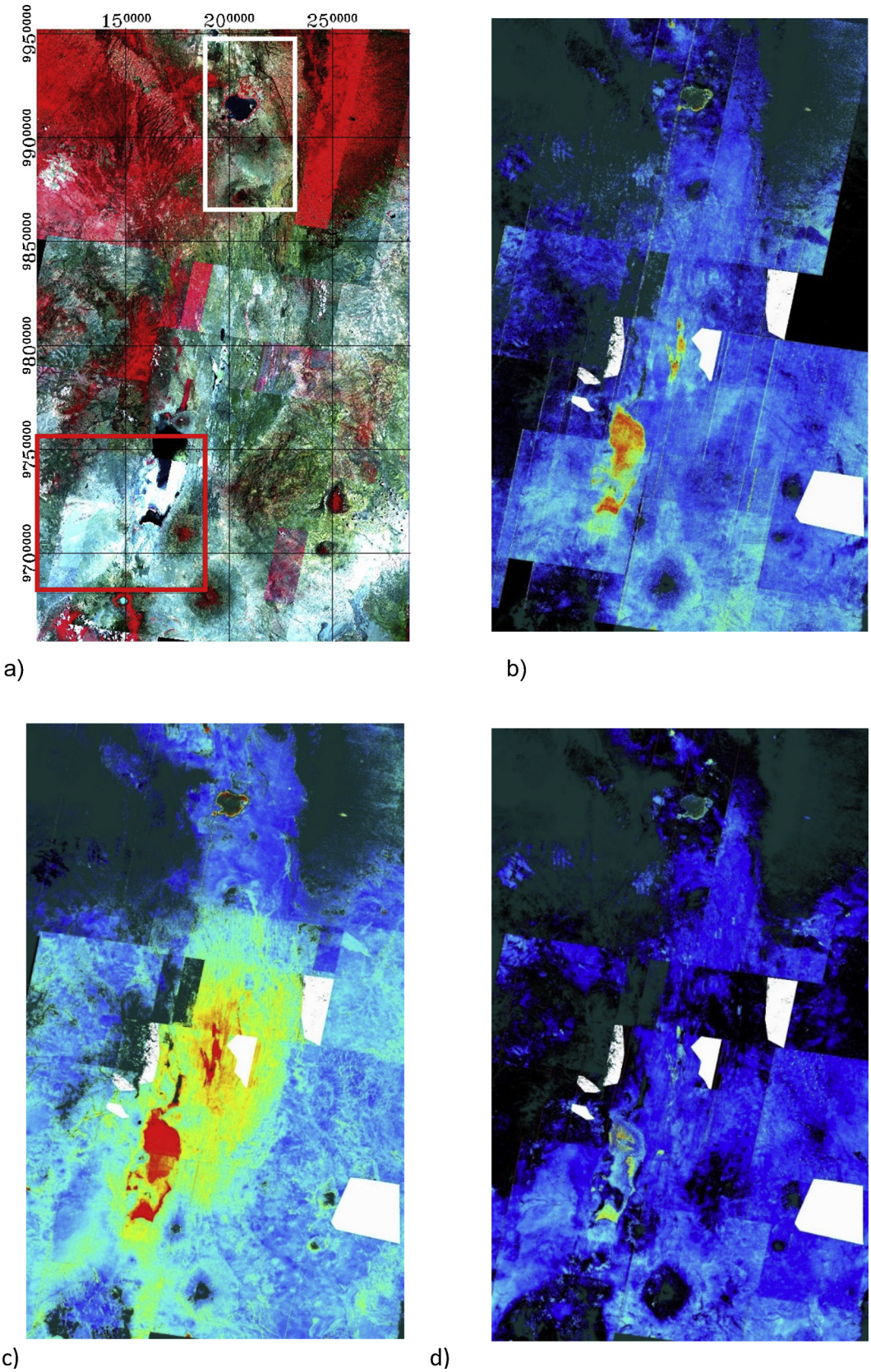

Fig. 5. a) The overall study area (see Fig. 4) showing the ASTER mosaic of Bands 3, 2 and 1 as the False color composite RGB image. The Kenyan geothermal fields study area (white box) and Lake Natron study area (red box) are shown; b) Opal content (linear histogram, band ratio values:0.95-1.1); c) MgOH-Carbonate (linear histogram, band ratio values:0.95-1.1 2.1-2.8); d) Ferrous Iron (linear histogram, band ratio values:0.95-1.10.75-1.2). (For interpretation of the references to colour in this figure legend, the reader is referred to the web version of this article).

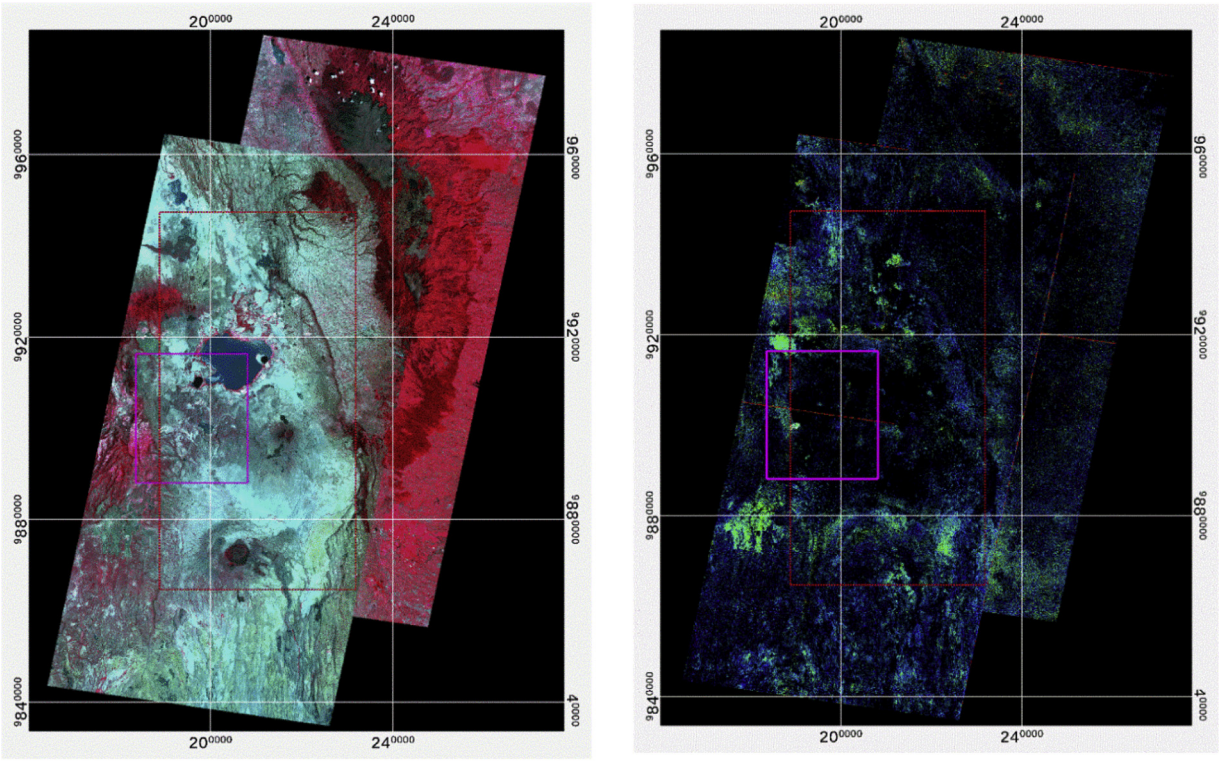

Fig. 6. a) FCC image (RGB: b3, b2, b1) of the northern Rift Valley (Kenyan geothermal study area = red box; Olkaria geothermal field area = magenta box); b) Argillic product (masked for high AlOH + vegetation) for same extents and boxes as a). (For interpretation of the references to colour in this figure legend, the reader is referred to the web version of this article).

addition, Fig. 4 indicates this investigations' overall study area (blue box) and the Kenyan geothermal study area (red box) in the northern part of the East African Rift. The Tanzanian geology within the study area consists of Proterozoic migmatite, granite and metasedimentary complex, Archaean granite, granodiorite and greenstone (volcanic-sedimentary) sequences, overlain with more recent East African Rift associated Tertiary volcanics and Quaternary sediments (Legler et al., 2015) (Fig. 4). Various mineral deposits are also highlighted (symbols: half circles, squares, pentagons) for sedimentary, metamorphogenic and magmatic deposits of rare metals/REEs, precious stones and industrial materials respectively (Fig. 4). However for this study, the most relevant resources identified by (Legler et al., 2015) are the mineralized and hot geothermal resources (Fig. 4, cyan rectangle symbols) particularly on the margins of Lake Natron.

An issue regarding this feasibility mapping study was the limitation of ASTER scenes limited to 60 × 60 km (compared to Landsat's 180 × 180 kms) and availability of cloud free dry season ASTER acquisitions for day and night imagery. Attempts were made for mosaicking compositional products from day time acquired ASTER however the variable LST between different night time thermal image acquisitions precluded their mosaicking and restricted the study areas. A detailed study of the Lake Natron hot springs area using such night time LST is also shown in Fig. 4 (black box). Note that for Fig. 4 and those following, the coordinate datum and projection displayed in this study for both maps and ASTER imagery is defined by WGS 84, UTM Zone 37 South coordinates.

3. Datasets & methodology

3.1. ASTER VNIR-SWIR

ASTER level 2 products for day time surface reflectance (AST_07XT) and night time LST ("Surface Kinetic Temperature"; AST_08) were retrieved from the online Data Pool, courtesy of the NASA Land Processes Distributed Active Archive Center (LP DAAC), USGS/Earth Resources Observation and Science (EROS) Center, Sioux Falls, South Dakota, using Earth Explorer (https://search.earthdata.nasa.gov/search). Descriptions of these products are available via https://lpdaac.usgs.gov/dataset_discovery/aster/aster_products_table. It should be noted that this study used "Crosstalk" corrected surface reflectance (AST_07XT) to minimize the reflected light interference between the SWIR array detectors (Iwasaki and Tonooka, 2005). The equatorial location of the study area necessitated acquiring imagery to avoid seasonal effects and scenes with high vegetation cover, where possible. The 39 archived day time ASTER scenes chosen for this study were generally acquired during the dry season and outside the major rainy season of April til July. Cloud cover and their shadows were sometimes an issue and some scenes were avoided, partially mosaicked or later manually masked to exclude those areas. ASTER reflectance products were also chosen from acquisitions between 2000 and April 2007 before the SWIR sensor became unreliable.

ASTER mineral compositional information was calculated using band ratio and relative band depth parameters (Crowley et al., 1989), as described by (Cudahy, 2012). Masking was applied as described by (Cudahy, 2012) except the Normalized Vegetation Index (NDVI) was used instead of the B3/B2 ratio mask as applied by (Cudahy et al., 2016). Using the commonly applied NDVI (Myneni et al., 1995) approach for discriminating green vegetation and masking with a

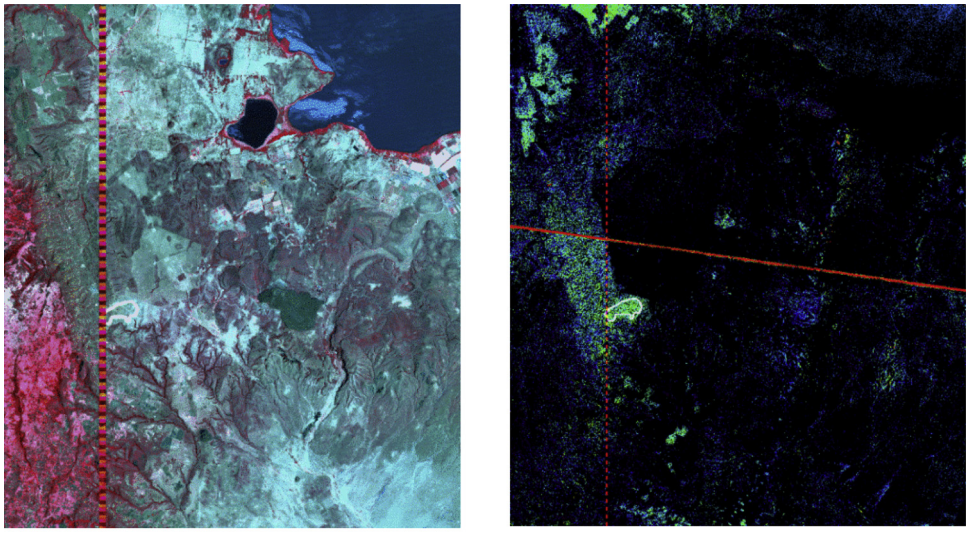

Fig. 7. a) Close up of FCC (magenta box Fig. 6 a); b) Anomalous argillic content (white polygon).

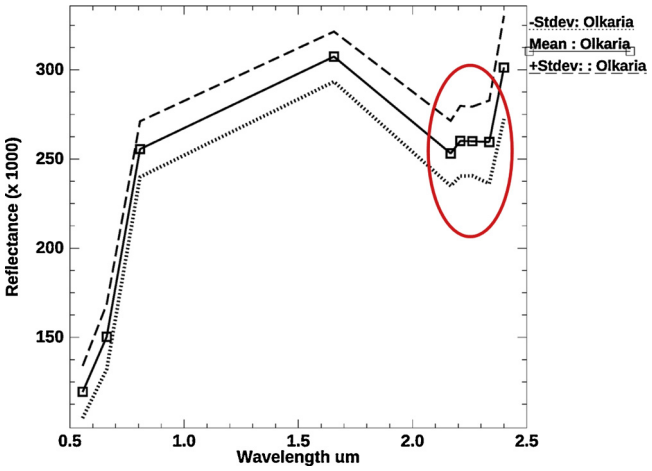

Fig. 8. Average VNIR-SWIR spectral signature of the anomalous defined area (Fig. 7 b).

threshold greater than 0.4 helped to improve the products consistency between different acquisitions (Myneni et al., 1995). No cross scene ASTER acquisition adjustment was made for temporal changes in season, residual atmospheric or solar angle effects. However the application of band ratios / relative band depth processing of reflectance products generally helped to reduce some of those variable illumination effects (Crowley et al., 1989).

ENVI™ (http://www.harrisgeospatial.com) and ERDAS ERMAPPER™ (https://www.hexagongeospatial.com) software were used to import, mosaic and perform band parameterization. The resulting compositional products were displayed using generally the histogram types and thresholds discussed in (Cudahy et al., 2016) and fully listed in (Cudahy, 2012). Further validation of the reliability of the band ratio and relative band depth parameter thresholds, assumed for the derived compositional products, was undertaken by calculating the statistical measures (average and standard deviation) of the spectral signatures of anomalies.

3.2. ASTER TIR

To optimize and enhance any geothermal temperature anomaly, a technique and software was developed by Ulusoy (Ulusoy et al., 2012) and applied to correct the ASTER LST imagery for elevation, aspect and slope temperature effects. This algorithm has been previously successfully applied by van der Meer (van der Meer et al., 2014) for processing ASTER LST data within the La Pacana caldera, Chile. The application of the Ulusoy's topographic LST technique requires the conversion of SRTM DEM data resampled to the same spatial resolution and extents as the ASTER LST imagery (e.g. 90 ms) and processing into slope and aspect products using ENVI™ software.

4. Results

Nine band ASTER VNIR-SWIR reflectance imagery within the study area was arranged using ERMapper™software as a mosaicked compilation, prioritizing those ASTER images with the greatest soil/outcrop exposure, least vegetation and cloud cover. The merged False Colour Composite (FCC) of the VNIR bands showed the issue of vegetation cover (e.g. bright red areas) and occasional clouds (bright white) (Fig. 5a). Nonetheless the two areas of interest show reasonable exposure (white and red boxes; Fig. 5a). Subsequent image products had vegetation and cloud masks applied to avoid any misinterpretation. Fig. 5b–d show examples of such ASTER compositional products with masks and assuming the linear stretches (blue = low relative content, red = high; dark green = vegetation mask; white = cloud). Where the parameter value is less a null value was assumed which either is represented by black or the underlying ASTER scene is visible and potentially supplies a valid product pixel value (Fig. 5 b–d). Note the low values for the Ferrous product (Fig. 5d) suggests that the MgOH-carbonate product (Fig. 5d) is more likely a ferrous lacking carbonate (e.g. calcite/travertine).

4.1. Kenyan geothermal fields

4.1.1. Mineral composition

A closer examination was undertaken for possible compositional or temperature spatial anomalies at the northern end of the Rift Valley within the study area (Fig. 5a, white box). Improved mosaicking results were enabled by using pairs of ASTER scenes acquired along the SSW descending orbit acquired within short time interval. However noticeable differences in vegetation cover between paths of different acquisition dates were apparent (Fig. 6a).

The argillic ASTER product was generated and showed some anomalous areas within this Olkaria field (green areas & white polygon,

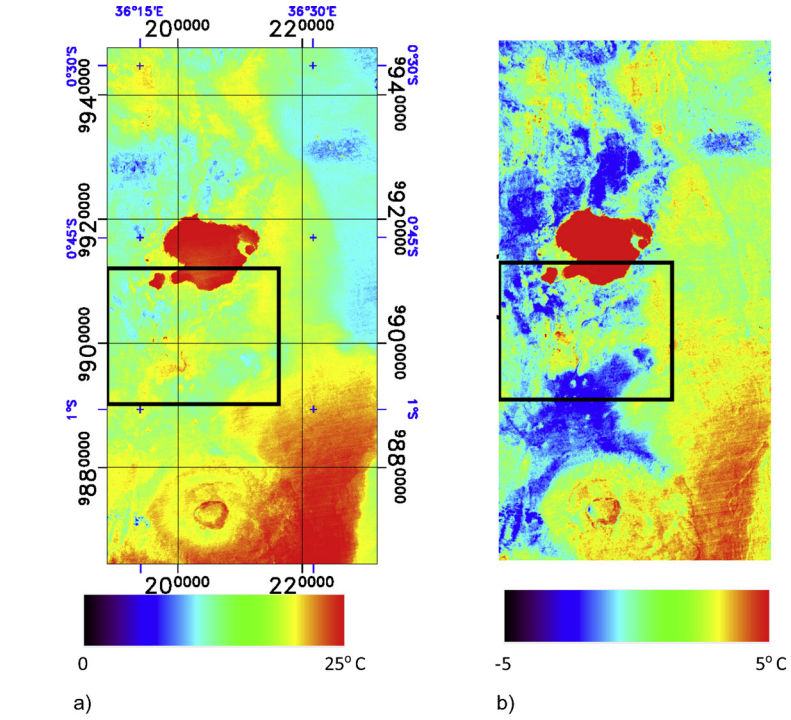

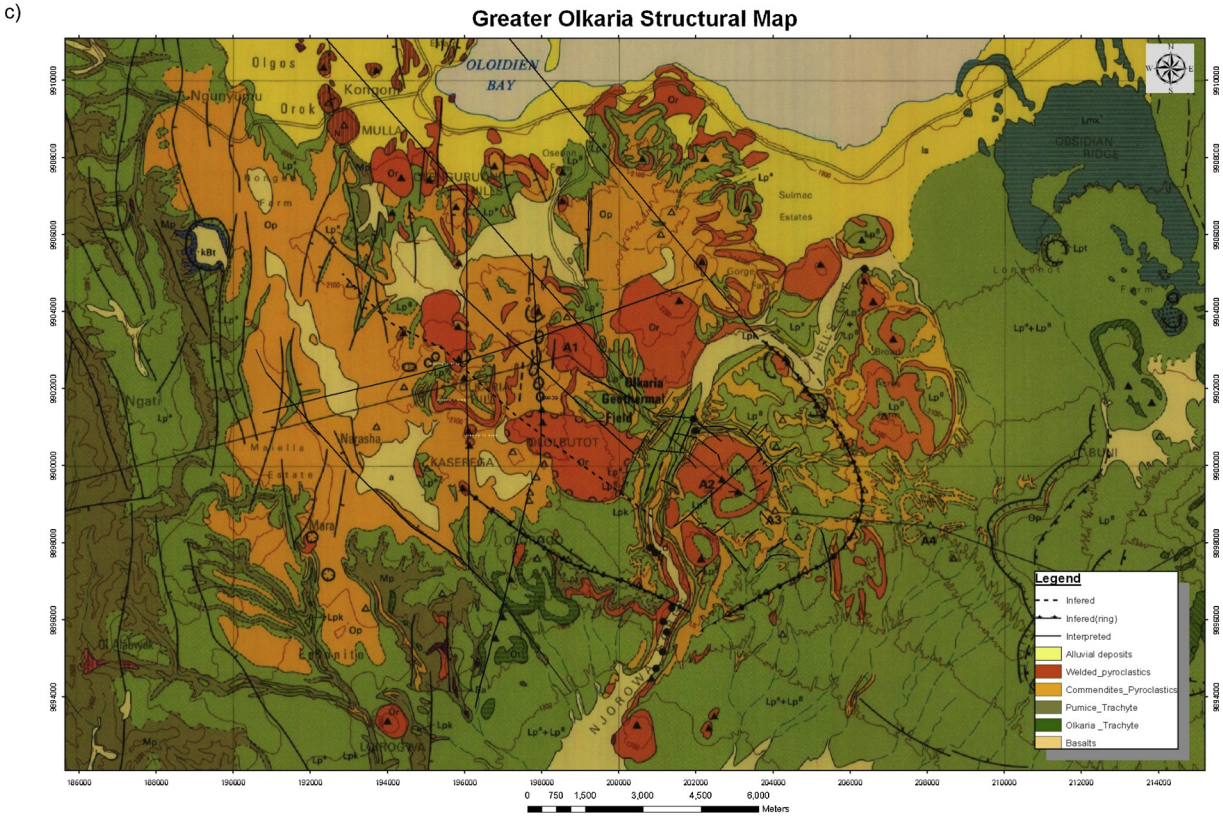

Fig. 9. Kenyan geothermal study area showing a) ASTER LST product; b) LST after elevation/slope/aspect adjustment. Both a) and b) show the outline (black box) of the detailed Olkaria geological map, c) (overleaf) the Olkaria Geothermal Field (courtesy of KenGen (https://www.kengen.co.ke/).

Fig. 7b). The average argillic index content within the white polygon sampled area was 1.1, well within the thresholds to validate this anomaly. The average spectral signature was also derived and shown in Fig. 8. The red ellipse in Fig. 8 highlights the expected argillic signature diagnostic by the relative reflectance of bands 5 and 7 (2.1 and 2.26 um). This compares favourably with the alunite USGS library spectral signature and its ASTER equivalent, displaying an absorption feature centred at 2.16 um or approximately ASTER band 5 (Fig. 2).

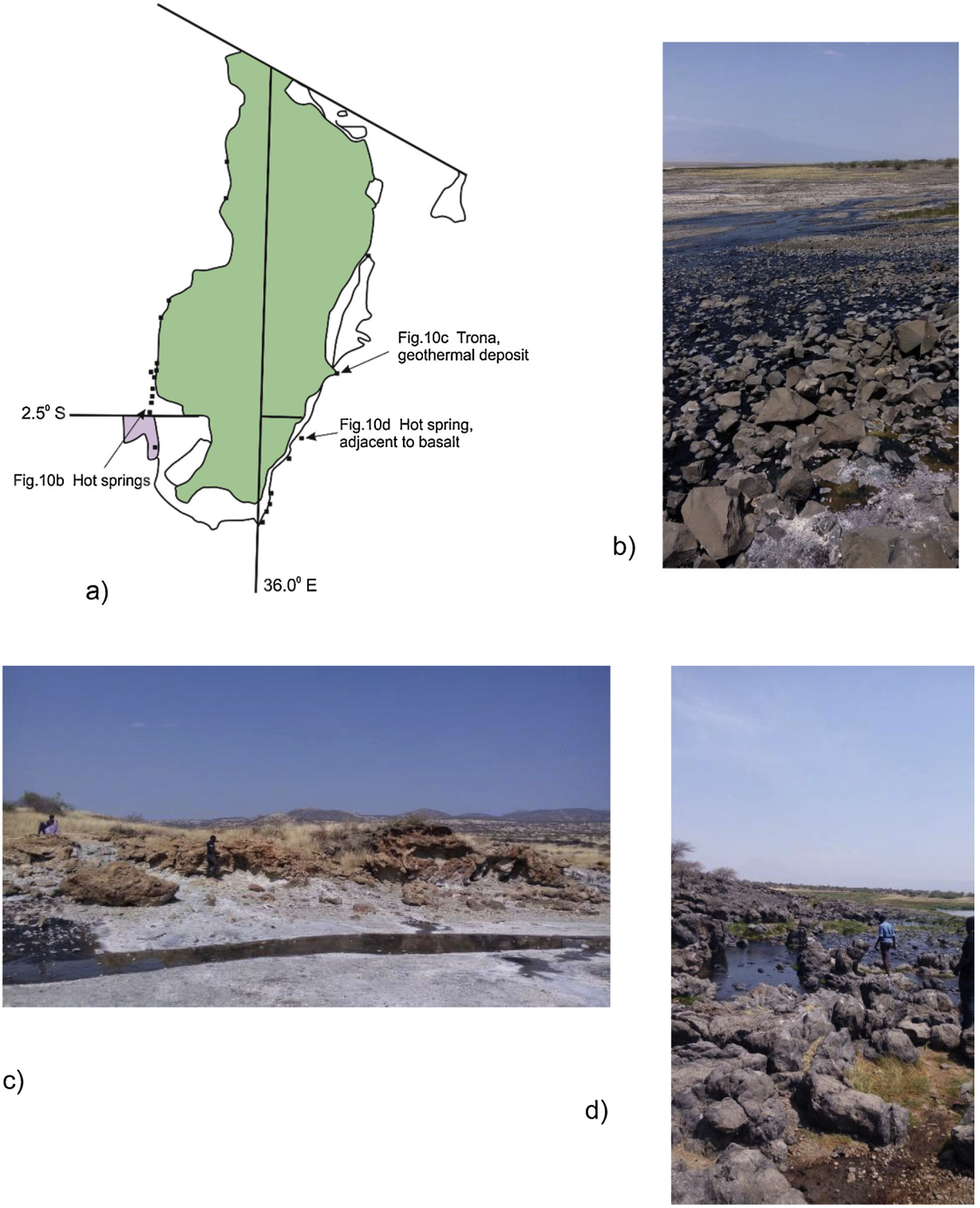

Fig. 10. Map of the Lake Natron and the locations for field photos b) – d).

4.1.2. Thermal products

The night time ASTER LST product (acquisition: 2007-02-19) was also examined within the Kenyan Olkaria geothermal field study area which had showed areas of anomalous clay mineralization (Fig. 7b). ASTER's LST showed a range of approximately 20–25 °C degrees related in part to topographic effects (Fig. 9a). However after the LST topographic elevation adjustment (Ulusoy et al., 2012) was applied, the range of LST reduced to approximately to 10 °C degrees (Fig. 9b). There were subtle LST anomalies apparent in the approximate area of the Olkaria field (200,000 E, 9,900,000 N; Black box - Fig. 9a) in the uncorrected ASTER LST however these were enhanced relative to the ambient background LST after the elevation correction was applied (Fig. 9b). It is also apparent in Fig. 9b that there were variable non topographic related LST anomalies immediately around the Lake Naivasha (205,000 E, 9,920,000 N) which are possibly due to variable outcropping pyroclastic and alluvial formations (Fig. 9c) as well as man-made infrastructure built on the lake shores, apparent within detailed Google Earth imagery. However the topographic corrected LST

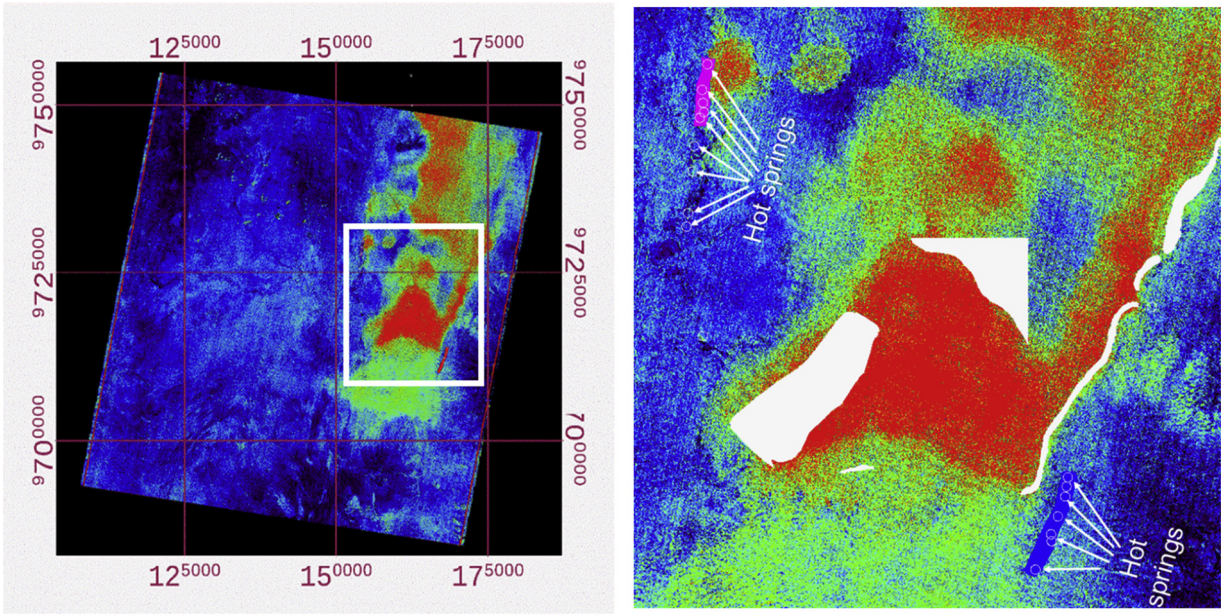

Fig. 11. a) Opal silica ASTER content product (histogram: linear, 0.95–1.1) with a close up area (white box) as shown in b). Blue = low, red = high interpreted content. White circles/arrows shown in Figure b) show hot spring localities (Fig. 10a). (For interpretation of the references to colour in this figure legend, the reader is referred to the web version of this article).
Region of Interest (ROI) spectral sample areas:
NW margin: purple area;
SE margin: blue area.
Tanzanian Geological Survey "Trona" mapping: white

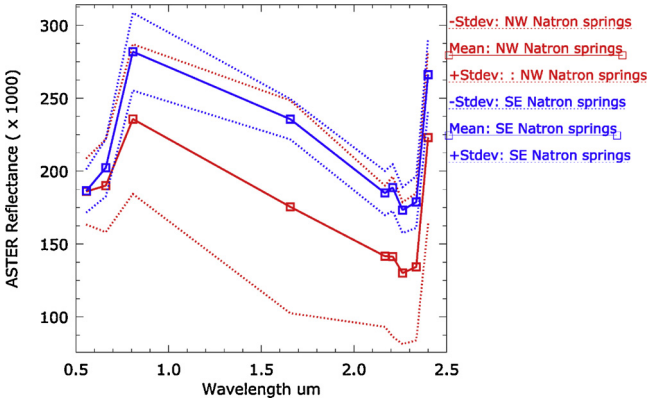

Fig. 12. Average ASTER spectral signature for NW and SE hot spring areas. Note the broad absorption feature in bands 7 and 8 (at 2.26 and 2.33 um).

anomalies within the central Olkaria geothermal field area were generally 2–3 °C above the background LST (200,000 E, 9,900,000 N; Fig. 9 b & c). The highest LST anomalies reached as high as 10° C above the background, likely to be related to the actual Olkaria geothermal plant infrastructure. Fig. 9c shows the geology of the Olkaria Geothermal Field (198000-20400mE, 990000–994000 mN), consisting of the pyroclastics, trachytes, and basalts (KenGen, *pers comm.*). Variations in such outcropping and near surface geological units with different physical properties (e.g. density/porosity, thermal conductivity) are also a potential source of LST anomalies (Coolbaugh et al., 2007; Eneva et al., 2006). Thermal inertial issues are not examined in this study but recommended for future investigations. However the detailed geological mapping shows several NW-SE and ENE-WSW faults, that may provide conduits for surface geothermal activity and possible mineralization of the host volcanic rocks (Fig. 9c). Further field work is recommended to ascertain whether the clay mineralization (Fig. 7b) relates to hydrothermal kaolinite/alunite content or the presence of weathered clays within the Olkaria field area. The discrimination of hydrothermal kaolinite (e.g. dickite) from weathered kaolinite is potentially discriminated by its crystallinity index based on its 2.16 um and 2.20 um doublet features (Hauff et al., 1990), however this is not possible at ASTER spectral resolution.

4.2. Lake Natron hot springs

4.2.1. VNIR-SWIR products

The hot springs surrounding the eastern and western margins of Lake Natron in Tanzania were examined. Many of the springs have been measured for temperatures, ranging between 30–50° C and associated with mineralized deposits Fig. 10a). The Lake Natron area has limited vegetation cover and good geological exposure (Fig. 10 b–d).

The opaline silica band ratio product (Table 1) derived from the ASTER acquisition 1-11-2005, showed the lake has anomalously high opaline silica present (Fig. 11a). Limited ASTER spectral signatures were available for identifying possible salts however some of the ASTER scenes also suggested the presence of water which can affect the spectral signature of any evaporate deposit. A close up view of the opal silica imagery (Fig. 11b) within one scene was assessed for its average spectral signatures within several of the hot spring field sites shown in Fig. 10 a–d (Fig. 11b, NW margin: magenta area; SE margin: blue area).

The averaged signatures (Fig. 12) were obtained from ROI areas on the north western and south eastern margins of Lake Natron (Fig. 11b). The average ASTER spectra from both hot spring areas (Fig. 12) compared approximately to what was expected for opaline silica related to the absorption feature apparent in bands 7 and 8 (Fig. 2). An average opal (band ratio) product index value of 1.03 for the mapped anomalies also indicate the chosen threshold for the display appears appropriate. However gypsum (Fig. 2) is another possible interpretation for these Lake Natron signatures. The anomalously high values shown for ASTER band 9 (~2.4 μm) is possibly the result of residual ASTER Crosstalk

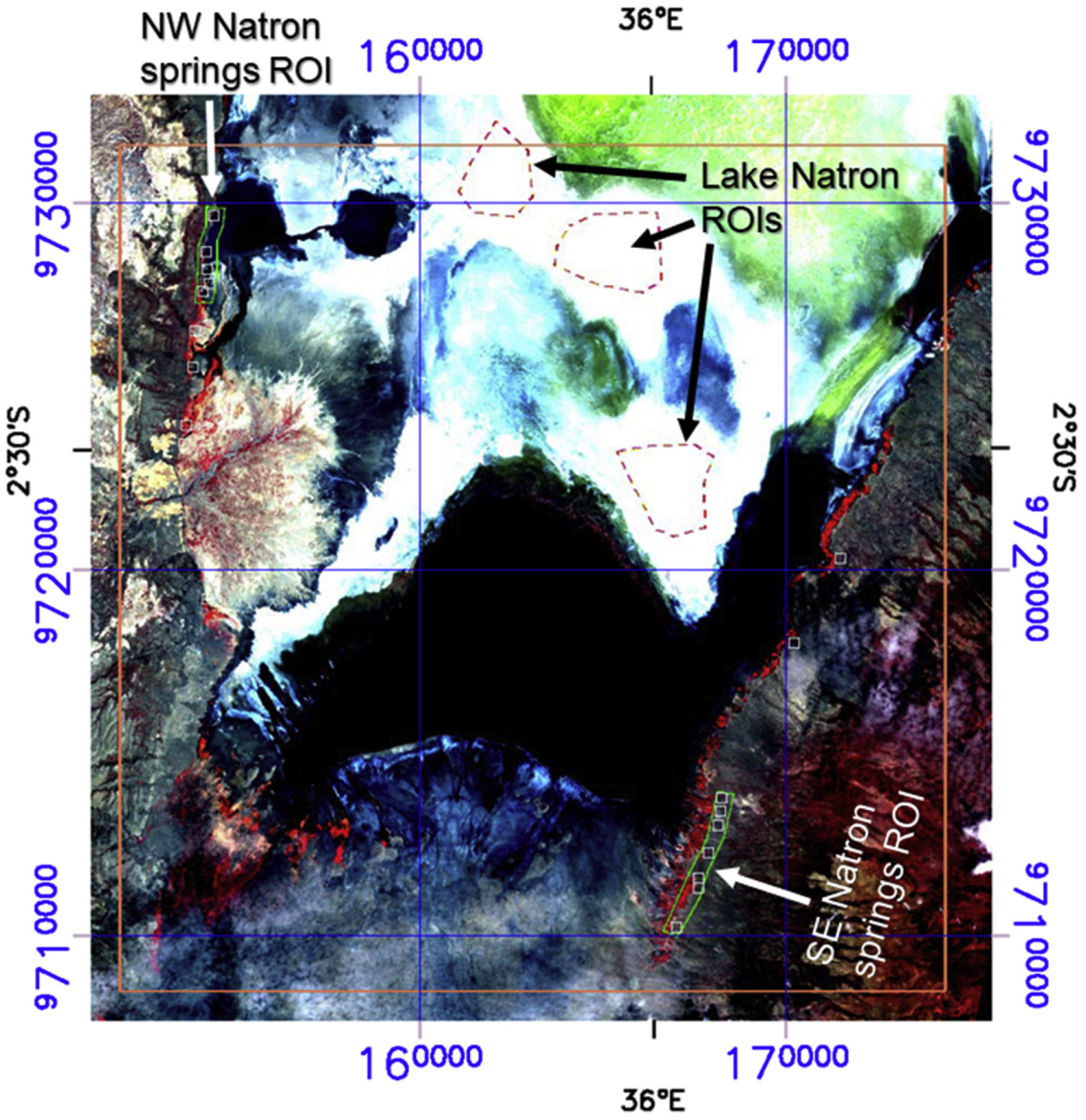

Fig. 13. ASTER False RGB 321 (acquisition: 1-11-2005) of the close up area in Fig. 11b, encompassing the southern part of Lake Natron. The mapped hot springs = white markers; NW and SE ROIs = green polygons; and Lake Natron "salt" bed ROI ASTER spectral sampling = dashed red polygons. (For interpretation of the references to colour in this figure legend, the reader is referred to the web version of this article).

issues that affects bands 5 and 9 (Iwasaki and Tonooka, 2005). Such residual Crosstalk issues have been observed in previous ASTER geological mapping studies, despite the use of Crosstalk corrected AST_07XT surface reflectance imagery (Hewson et al., 2015). Field spectral measurements, detailed sampling and possible XRD analysis would be useful to identify the actual mineralogy of these hot spring deposits and lake bed deposits.

More ROI/spectral training areas were defined to compare these hot spring spectral signatures with the lake bed signatures of Lake Natron (Fig. 13, dashed red polygon areas). The Lake Natron mean ROI spectral signatures showed a moderate to poor comparison with the equivalent ASTER opal (Fig. 14). Library signatures of the previously mapped mineral trona (Fig. 11b), as well as the geothermal borate mineral, tincalconite (Kratt et al., 2006b) also showed some but limited comparison spectrally (Fig. 14). Hull removed continuum reflectance was used to display and enhance possible SWIR absorption features in Fig. 14. A possible explanation of the limited comparison between the Lake Natron ASTER and library spectra could be the issue of spectral mixing of these different minerals within the 30 m ASTER pixels, as well as possible diminished spectral contrast of any absorption features from any presence of moisture (Fig. 14).

4.2.2. TIR products

The night time ASTER LST imagery (acquisition: 2014-09-09)and its corresponding elevation adjusted product, showed no clear thermal anomaly for the hot springs on the NW and SE margins of Lake Natron (Fig. 15 a & b). However the adjusted LST product suggested a more discernible boundary along the trend of the NW and SE hot springs, possibly related to changes in subsurface thermal properties adjacent to Lake Natron (Fig. 15b).

5. Discussion

This mapping study using day and night ASTER imagery shows its ability to discriminate surface composition and temperature features over a large area. Attempting identification of the mineralogy and sources for any thermal anomalies indicated several challenges. ASTER's SWIR bands suggested the presence of argillic, possibly alunite

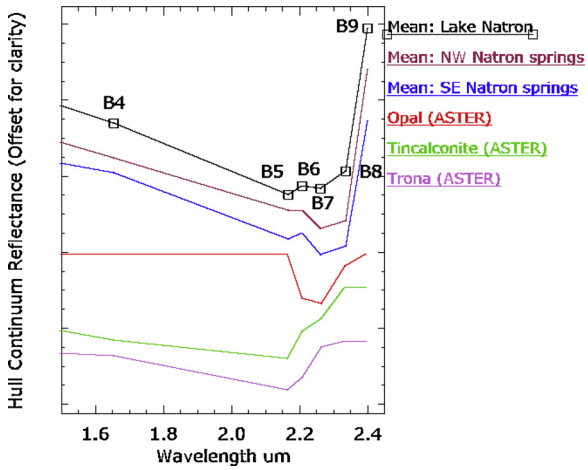

Fig. 14. Comparison of Lake Natron hot springs ROIs mean ASTER SWIR spectra (Fig. 12) with Lake Natron evaporites or "salt" bed ROIs (Fig. 13) and with ASTER resampled USGS library spectral examples for opaline silica, and borate minerals, tincalconite and trona (Baldridge et al., 2009). Hull removed continuum reflectance was displayed to enhance possible absorption features.

clays, opaline silica / gypsum spring and evaporate mineralization within the study areas. This compares with the straight forward geothermal ASTER mapping interpretation achieved with the Fish Lake geothermal and Brady's Hot Springs fields in Nevada, USA (Coolbaugh et al., 2007; Littlefield and Calvin, 2014). It however appears that there is a diversity in the types of alteration and evaporate minerals associated with different geothermal fields. Evaporites in particular may or may not be associated with geothermal activity, including minerals such as borates, gypsum, travertine and trona and tincalconite which have variable diagnostic spectral features at ASTER spectral resolution (Coolbaugh et al., 2007; Kratt et al., 2006b; Littlefield and Calvin, 2014). Having *a priori* information to use in conjunction with the interpretation of ASTER imagery, or at least field sampling and analysis following the preliminary image processing, appears important to reduce the ambiguities involving the identification of any alteration and/or evaporite mineralogy.

LST anomalies appear coincident with the Olkaria geothermal fields (Fig. 9b) but are not present for the temperatures observed for the relatively small Lake Natron springs (Fig. 10 a–d). A significant caveat for the thermal imagery is the 90 m pixel spatial resolution of the ASTER sensor. Any moderately sized hot spring needs to have a large thermal contrast above the ambient background in order to produce a detectable LST within several 90 × 90 m ASTER pixels. However it appears that an overall increase ground temperature is detectable by night time topographic corrected ASTER LST, within the Olkaria geothermal field measured at 2–3 °C above the surrounding background. As with the comment above regarding *a priori* or field validation of mineral composition, there is a need to have a ground based knowledge of the sizes and properties of surface fumaroles/hot springs for a reliable map interpretation.

Careful selection of ASTER scene acquisitions and masking for vegetation was also found to be important. No correction or masking for dry vegetation has been applied and this could not be possible using the green vegetation NDVI masking. Variable dry grass/bare soil exposure between different ASTER scenes, even from dry season acquisitions, appears apparent between different years (*e.g.* El Nino, (Cudahy et al., 2016)). It appears there are better mosaicked results obtained from ASTER scenes acquired along the same contemporaneous orbits that avoid temporal changes in vegetation, although this limits the effective map product swath width to 60 km.

The issue of the accuracy for ASTER derived mineral map products has been described by (Cudahy (2012)) based on comparison with ground observations and hyperspectral image data. The particular map products used in the this study were described as having "moderate" accuracy in (Cudahy (2012))'s Australian application study. Hewson

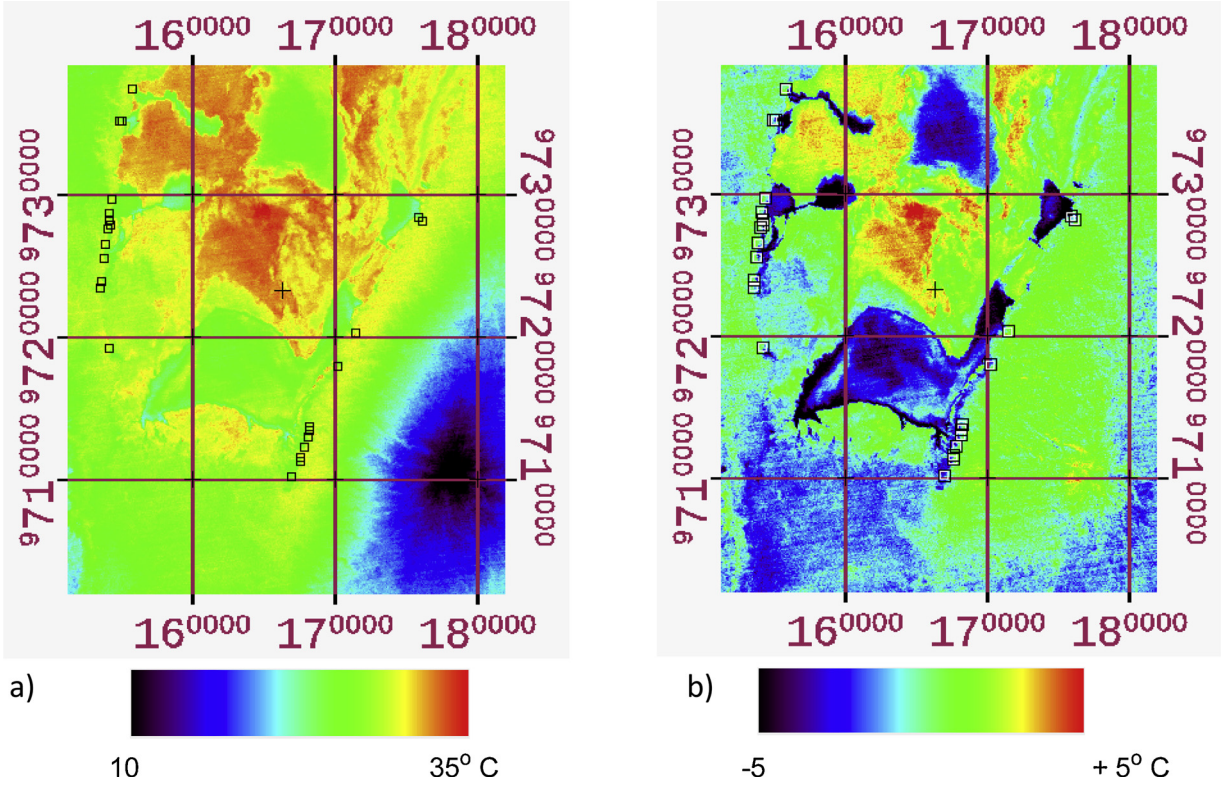

Fig. 15. a) ASTER LST product over Lake Natron (Fig. 11a, white box); b) Elevation adjusted LST. The black marker boxes in a) and in b) correspond to the hot spring localities (Fig. 10 a–d).

(Hewson et al., 2018) further examined the seasonal repeatability of map products over different acquisition years within the Kenyan/Tanzanian border area, and showed differences in the absolute compositional index values although the regional and spatial trends were still apparent. A close up examination of the VNIR imagery also suggested that fireburn scars were present and a likely source of some image boundary discrepancies (Hewson et al., 2018).

6. Conclusion and recommendations

The results in this study showed the potential for mapping some of the geothermal and evaporite associated minerals and temperature anomalies using ASTER imagery within the East African Rift Valley straddling Tanzania and Kenya. In particular, occurrences of geothermal indicator minerals such as trona, opaline silica and argillic clays appeared to be mapped by ASTER within the study areas. Also LST anomalies were identified by ASTER night time imagery within the Kenyan Olkaria Geothermal Field, as previously described by (Romaguera et al., 2018). No clear LST anomalies however were detected from the Lake Natron hot springs, possibly related to the moderate temperatures measured at 30–50° C, and ASTER TIR's coarse spatial resolution.

Further investigation of this satellite borne exploration technique is needed, including more field site observations, temperature measurements and sampling for later spectral and X ray diffraction mineral analysis. Field validation work is needed to understand the sources of mineral and temperature anomalies that are not likely to be related to geothermal activity. In particular, potential false anomaly issues need to be checked arising from vegetation cover, water bodies, soil moisture/composition, and thermal inertial properties of the regolith / outcrops (Coolbaugh et al., 2007; Eneva et al., 2006). An assessment of the spatial dimensions of hot springs or other near surface geothermal expressions would also estimate the geothermal detection limits of ASTER's 90 m TIR imagery. Overall this study's location provides a useful test site for evaluating such day/night time satellite remote sensing with known Kenyan geothermal fields and Tanzanian hot springs. The use of such imagery offers the potential for cost-effective and large scale regional mapping, that can complement geophysical/geochemical techniques applied for more detailed and focused geothermal exploration.

Acknowledgements

The original ASTER imagery was made freely available following over seven successive years of VNIR, SWIR, TIR image acquisition and product distribution by the US NASA and Japan's METI organizations. In particular the authors are appreciative for data access from the NASA Land Processes Distributed Active Archive Center (LP DAAC). Access and use of geological published mapping by the Kenyan and Tanzanian Geological Surveys is also gratefully acknowledged. Much appreciation is expressed also to the KenGen organization of Kenya for providing the detailed Greater Olkaria Structure/Geological (https://www.kengen.co.ke/). Thanks are also given to Benno Masselink of University of Twente – ITC for the enhancement of several figures.

References

Abrams, M., 2000. The Advanced Spaceborne Thermal Emission and Reflection Radiometer (ASTER): data products for the high spatial resolution imager on NASA's Terra platform. Int. J. Remote Sens. 21 (5), 847–859.

Abrams, M., Tsu, H., Hulley, G., Iwao, K., Pieri, D., Cudahy, T., Kargel, J., 2015. The Advanced Spaceborne Thermal Emission and Reflection Radiometer (ASTER) after fifteen years: Review of global products. Int. J. Appl. Earth Obs. Geoinf. 38, 292–301.

ACP-INT: Secretariat of African, 2019. Caribbean and Pacific Group of States Mining Data Bank. http://mines.acp.int/pays_images/KE/Geol_Gito.JPG.

Adams, J.B., Filice, A.L., 1967. Spectral reflectance 0.4 to 2.0 microns of silicate rock powders. J. Geophys. Res. 72, 5705–5715.

Baldridge, A.M., Hook, S.J., Grove, C.I., Rivera, G., 2009. The ASTER spectral library version 2.0. Remote Sens. Environ. 113, 711–715.

Coolbaugh, M.F., Kratt, C., Fallacaro, A., Calvin, W.M., Taranik, J.V., 2007. Detection of geothermal anomalies using Advanced Spaceborne Thermal Emission and Reflection Radiometer (ASTER) thermal infrared images at Bradys Hot Springs, Nevada, USA. Remote Sens. Environ. 106, 350–359.

Crowley, J.K., Brickley, D.W., Rowan, L.C., 1989. Airborne imaging spectrometer data of the Ruby Mountains, Montana: mineral discrimination using relative absorption band-depth images. Remote Sens. Environ. 29, 121–134.

Cudahy, T.J., 2012. Australian ASTER Geoscience Product Notes, Version 1, 7th August, –CSIR0. ePublish No. EP-30-07-12-44. .

Cudahy, T.C., Caccetta, M., Thomas, M., Hewson, R., Abrams, A., Kato, M., Kashimura, O., Ninomiya, Y., Yamaguchi, Y., Collings, S., Laukamp, C., Ong, C., Lau, I., Rodger, A., Chia, J., Warren, P., Woodcock, R., Fraser, R., Rankine, T., Vote, J., de Caritat, P., English, P., Meyer, D., Doescher, C., Fu, B., Shi, P., Mitchell, R., 2016. Satellite-derived mineral mapping and monitoring of weathering, deposition and erosion. Nat. Sci. Rep. 6https://doi.org/10.1038/srep23702. Article number: 23702.

Darge, Y.M., Hailu, B.T., Muluneh, A.A., Kidane, T., 2019. Detection of geothermal anomalies using Landsat 8 TIRS in Tulu Moye geothermal prospect, Main Ethiopian Rift. Int. J. Appl. Earth Obs. Geoinf. 74, 16–26.

Eneva, M., Coolbaugh, M., Combs, J., 2006. Application of satellite thermal infrared imagery to geothermal exploration in East Central California. Geotherm. Resour. Counc. Trans. 30, 407–412.

Hauff, P.L., Kruse, F.A., Thiry, M., 1990. Characterization of interstratified kaolinite/smectite clays using infrared reflectance spectroscopy (1.2–2.5 μm). In: Proc. Geochemistry Of The Earth's Surface And Of Mineral Formation 267, 2nd International Symposium. July, 2–8, 1990, Alx En Provence, France. pp. 267–270.

Hecker, C.A., Hewson, R.D., Setianto, A., Saepuloh, A., van der Meer, F.D., 2017. Multi-source remote sensing data analysis for geothermal targeting on Flores island. In: Proc. 5th Indonesia International Geothermal Convention & Exhibition (IIGCE) 2017. 2–4 August 2017, Jakarta, Indonesia. Jakarta. pp. 1–7.

Hewson, R.D., Cudahy, T.J., Mizuhiko, S., Ueda, K., Mauger, A.J., 2005. Seamless geological map generation using ASTER in the Broken Hill-Curnamona province of Australia. Remote Sens. Environ. 99 (1–2), 159–172 2005.

Hewson, R., Robson, D., Mauger, A., Cudahy, T., Thomas, M., Jones, S., 2015. Using the Geoscience Australia-CSIRO ASTER maps and airborne geophysics to explore Australian geoscience. J. Spatial Sci. 60 (2), 2015. https://doi.org/10.1080/14498596.2015.979891.

Hewson, R.D., van der Werff, H., Mshiu, E., Alkema, D., van der Meer, F., 2018. Supplementing geological mapping with aster In East Africa. In: In Press, Proc. IEEE International Geoscience and Remote Sensing Symposium. 23–27, July 2018, Valencia, Spain. pp. 4.

Hunt, G.R., Ashley, R.P., 1979. Spectra of altered rocks in the visible and near infrared. Econ. Geol. 74, 1613–1629.

Iwasaki, A., Tonooka, H., 2005. Validation of a crosstalk correction algorithm for ASTER/SWIR. IEEE Trans. Geosci. Remote. Sens. 43 (12), 2747–2751.

Kratt, C., Calvin, W., Coolbaugh, M., 2006a. Geothermal exploration with Hymap hyperspectral data at Brady–Desert Peak, Nevada. Remote Sens. Environ. 104, 313–324.

Kratt, C., Coolbaugh, M., Calvin, W., 2006b. Remote detection of quaternary borate deposits with ASTER satellite imagery as a geothermal exploration tool. Geotherm.Resour. Counc. Trans. 30, 435–440.

Legler, C., Barth, A., Knobloch, A., Mruma, A.H., Myumbilwa, Y., Magigita, M., Msechu, M., Ngole, T., Stanek, K., Boniface, N., Kagya, M., Manya, S., Berndt, T., Stahl, M., Gebremichael, M., Dickmayer, E., Repper, C., Falk, D., Stephan, T., 2015. Minerogenic Map of Tanzania and Explanatory Notes for the Minerogenic Map of Tanzania 1:1,5 M. Geol. Surv. Tanzania.

Littlefield, E.F., Calvin, W.M., 2014. Geothermal exploration using imaging spectrometer data over Fish Lake Valley, Nevada. Remote Sens. Environ. 140, 509–518.

Lyon, R.J.P., Burns, E.A., 1963. Analysis of rocks and minerals by reflected infrared radiation. Econ. Geol. 58, 274–284.

Myneni, R.B., Hall, F.G., Sellers, P.J., Marshak, A.L., 1995. The interpretation of spectral vegetation indexes. IEEE Trans. Geosci. Remote. Sens. 33, 481–486.

Romaguera, M., Vaughan, R.G., Ettema, J.A., Izquierdo-Verdiguier, E., Hecker, C.A., van der Meer, F.D.A., 2018. Detecting geothermal anomalies and evaluating LST geothermal component by combining thermal remote sensing time series and land surface model data. Remote Sens. Environ. 204, 534–552.

Simiyu, S.M., Keller, R., 2000. Seismic monitoring of the Olkaria Geothermal area, Kenya Rift valley. J. Volcanol. Geotherm. Res. 95 (1), 197–208. https://doi.org/10.1016/S0377-0273(99)00124-9.

Ulusoy, I., Labazuy, P., Aydar, E., 2012. STcorr: An IDL code for image based normalization of lapse rate and illumination effects on night time TIR imagery. Comput. Geosci. 43, 63–72.

Urai, M., Muraoka, H., Nasution, A., 2002. Satellite remote sensing data and their interpretations for geothermal application: a case study on the Ngada District, central Flores, Indonesia. Bull. Geol. Surv. Jpn. 53, 99–108.

van der Meer, F., Hecker, C., van Ruitenbeek, F., van der Werff, H., de Wijkerslooth, C., Wechsler, C., 2014. Geologic remote sensing for geothermal exploration: a review. Int. J. Appl. Earth Obs. Geoinf. 33, 255–269.

Vincent, R.K., Thomson, F., 1972. Spectral compositional imaging of silicate rocks. J. Geophys. Res. 77 (14), 2465–2472.

Vincent, R.K., Rowan, L.C., Gillespie, R.E., Knapp, C., 1975. Thermal-infrared spectra and chemical analyses of twenty-six igneous rock samples. Remote Sens. Environ. 4, 199–209 In Proc. International Geoscience and Remote Sensing Symposium (IGARSS), 9–13 July. 3p.

Wang, K., Jiang, Q., Yu, D., Yang, Q., Wang, L., Han, T., Xu, X., 2019. Detecting daytime and nighttime land surface temperature anomalies using thermal infrared remote sensing in Dandong geothermal prospect. Int. J. Appl. Earth Obs. Geoinf. 80, 196–205.